# Defect-rich ZnO nanorod arrays for efficient solar water splitting

Article (Accepted Version)

# Defect-Rich ZnO Nanorod Arrays for Efficient Solar Water Splitting

Daniel Commandeur, Grant Brown, Edward Hills, John Spencer and Qiao Chen*

Chemistry Department, School of Life Sciences, University of Sussex, Brighton, BN1 9QJ, UK

*Corresponding author. Email: qiao.chen@sussex.ac.uk

Abstract

A novel ultra rapid synthetic method for the production of vertically aligned ZnO nanorod (NR) arrays has been demonstrated, using a microwave assisted chemical bath deposition method. High quality NR arrays with controllable film thickness were achieved with fine control of the growth conditions. A fast growth rate averaging 0.9 μm $h^{-1}$ was achieved in comparison to 0.1 μm $h^{-1}$ from the conventional chemical bath deposition. The MW synthesised NRs have a high level of n-type doping, which confers excellent photoelectrochemical performance. In comparison with the typical chemical bath deposition synthesised NRs, the ultra-fast MW synthesised NRs offer 3 times more efficient in PEC water splitting. The population densities and electronic states of these defects were monitored using photoluminescence spectroscopy and electrical impedance spectroscopy. The dopant level was further controlled by thermal annealing in air and an optimised density of $1.68 \times 10^{19}$ $cm^{-3}$ was achieved after annealing at 500°C. This in turn led to a twofold increase in PEC efficiency to 0.31% with a photocurrent density of 0.705 mA $cm^{-2}$ at 1.23 V vs RHE, which is one of the best performances from similar ZnO NR structures.

**Keywords:** Ultra rapid growth, ZnO nanorods, Photocatalysis, Water splitting, Defects control, n-type doping

## 1 Introduction

The ambitious targets set in the landmark Paris Agreement in 2015 call for an increased push for renewable alternatives to fossil fuels in order to limit global warming to 2°C.[1] Recently, the 48th session of the Intergovernmental Panel on Climate Change (IPCC-48) recognised that it is still possible to achieve this target, although it requires unprecedented technology transitions within the next decade.[2] Photoelectrochemical (PEC) water splitting has been researched extensively for efficient harvesting of solar energy in $H_2$ gas.[3–5] A number of nanostructured metal oxide semiconductors, such as $TiO_2$ and ZnO, are suitable for this application, due to their wide band gap and stability in water.[6,7] A higher electron mobility of 205 $cm^2\ V^{-1}\ s^{-1}$ and longer minority carrier diffusion length give ZnO the advantage over $TiO_2$.[8] Much literature has been published employing a number of different strategies to enhance the photoconversion efficiency through doping,[9–11] sensitising[12–14] and plasmonic enhancement.[15–17] For example, Cu, V and N doped ZnO nanorods have shown significant enhancement in either UV or visible light sensitivity.[18–20] One of the most promising ZnO structures, vertically aligned nanorod arrays (NRs), offer large surface area and effective charge transport. However, ZnO NR arrays are synthesised slowly, at a typical growth rate of 0.1~0.5 μm $h^{-1}$, through either chemical bath deposition CBD, hydrothermal method or chemical vapour deposition.[21–23] Both the CBD method used by Meng Wang *et al.*[20] and the hydrothermal synthesis by Chenglong Zhang *et al.*[18] and Li Cai *et al.*[19] take as long as 24 hours.

Metal oxide nanowires are highly effective materials for solar water splitting.[24] ZnO nanowires provide the basis for highly efficient photoanodes, especially those sensitized with visible light absorbing materials such as CdS and $ZnFe_2O_4$.[25] Therefore, improving the pure ZnO properties, as achieved in this work, has the potential to impact a wide field of junction applications.

Here we report for the first time an Ultra Rapid Microwave Assisted Deposition (URMAD) of vertically aligned ZnO NR arrays applied as a photoanode for the photolysis of water. This method uses the synergy of efficient microwave (MW) dipole heating and conductive heating

of the system. Not only were NRs grown in a fraction of the time compared to conventional methods, the synthesis led to high density of surface defects with increased n-type doping. Consequently, the MW NRs showed a great increase in photoconversion efficiency for water splitting compared to the CBD sample.

Producing nanostructures using microwave (MW) heating has drawn recent attention in literature due to rapid, efficient and uniform dipole heating in aqueous solution.[26–28] The challenge of this rapid method is to control the morphology and the uniformity of the NR crystals. Microwave assisted synthetic methods have been applied to a number of ZnO nanostructures.[29–34] Vertically aligned ZnO NR arrays have appeared recently in the literature with limited control of morphology. They were used as a photocatalyst[35] or in a gas ionization sensor.[36] In both cases enhanced electronic properties were observed and this was attributed to increased oxygen vacancies from rapid crystallisation.

Oxygen vacancies ($V_O$) and zinc interstitials ($Zn_i$) are often suggested to be responsible for n-type doping in ZnO and its photocatalytic activity.[35,37] However, acceptor defects, such as zinc vacancies ($V_{Zn}$) contribute to p-type doping.[38,39] An appropriate n-type doping with very little p-type doping gives higher water splitting ability due to faster charge transfer to the electrolyte[40]. On the other hand, the p-type defects can have a significant negative impact due to a shift of the flat-band potential towards the valence band. In this work, the abundance of individual crystal defects are quantitatively analysed using photoluminescence (PL) spectroscopy and electrical impedance spectroscopy (EIS) measurements. This allowed greater control of the doping through annealing at a range of temperatures in air, yielding a significantly higher PEC efficiency at 500°C.

In this paper, a novel ultra rapid MW assisted chemical bath deposition method for the growth of ZnO NR arrays is presented and their solar water splitting ability is compared to a conventional CBD method. The NR arrays show high density of native defects, which is responsible for the increase in PCE conversion efficiency over the conventional CBD NRs by a factor of 3. The populations of these defects were then controlled using thermal annealing in air at

various temperatures to double the efficiency achieved. This yielded a photocurrent density of $0.893\,\mathrm{mA\,cm^{-2}}$ at $1\,\mathrm{V}$ potential bias vs KCl saturated Ag/AgCl reference electrode.

## 2 Experimental method

### 2.1 Synthesis of ZnO nanorods

All chemicals used were purchased from Sigma Aldrich with no further purification. Transparent conductive Fluorine-doped Tin Oxide (FTO) sheet glass was used as the substrate, cut into sample sizes of 1 × 3 $cm^2$. The substrate was cleaned by sonication successively in acetone, isopropanol then deionised (DI) water, for 20 minutes each, followed by drying in air. The seeding solution was prepared by dissolving 0.219 g zinc acetate and 0.6 g polyvinyl alcohol (PVA) for increased viscosity in 10 ml of DI water. The seeding solution was spin coated on the FTO glass for 3 minutes at 500 RPM. After this, the substrate was annealed in air for 20 minutes at 500°C to convert the zinc acetate into zinc oxide nano seeds.[41]

In the URMAD method, the seeded substrate was placed in a 35 ml microwave vessel with 20 ml growth solution, 1:1 hexamethylnetetramine (HMT) and zinc nitrate $Zn(NO_3)_2$ at a concentration of 40 mM. The microwave (Discover SP, CEM) was set to 100°C for 30 minutes at a power of 100 W, no stirring was used to avoid disturbing the crystal growth. The process was repeated four times (total 2 hours) for film thickness of around 2 μm. Following growth, all samples were rinsed with DI water. Annealing in air was performed using a tube furnace for 30 minutes at 300°C, 400°C, 500°C and 550°C to optimise crystal defect concentration. For comparison, a previously developed CBD technique was also used.[41] To achieve similar 2 μm NRs in CBD, the seeded substrate was placed in a beaker with 100 ml growth solution at 90°C for 16 hours.

## 2.2 Structural and physical characterization

The cross sectional and surface morphologies were observed using scanning electron microscopy (SEM, JSM820M, Jeol). The nanorod length and diameters were measured from SEM images using Image J software (National Institutes of Health, USA). The crystallinity and structural orientation of the nanostructures were analysed by powder x-ray diffractometer (XRD, Siemens D500). The reaction temperatures were recorded by FLIR ONE thermal camera and processed via the corresponding Android application.

## 2.3 Water splitting and optoelectronic measurement

PEC water splitting performances were measured using a standard 3 electrode set up. A KCl saturated Ag/AgCl electrode was used as the reference and platinum foil was used as the counter electrode. ZnO NR arrays grown on FTO-glass substrate were used as the photoanode. A potentiostat (EA163, eDAQ) was used to control the voltage bias and to measure the photocurrent. The voltage was scanned from -0.6 to 1.2 V and the electrolyte used in the PEC cell was 0.5 M $Na_2SO_4$. No additional scavenging chemicals were added to the electrolyte. A calibrated 100 mW/cm$^2$ solar simulator (Oriel LCS-100, Newport) with built-in 1.5 G filter used as the light source. The photoabsorption spectra used to calculate the band gap with Tauc plots were examined using a UV-Vis spectrophotometer (Thermospectronic UV 300) and the crystal defects were characterised using PL spectra recorded with a fluorescence spectrometer (Perkin Elmer LS 45). Finally EIS measurements were performed using an electrochemical controller (Palm Sens 3, PalmSens BV). Nyquist (illuminated) and Mott-Schottky (dark) plots were processed using PSTrace 4.5 (PalmSens BV).

## 3 Results and discussion

### 3.1 Morphology and crystal structure of URMAD synthesised nanorods

A clear benefit from the novel MW synthetic method is the efficient delivery of heat into the growth solution. The thermal image in the MW heating process, Fig. 1A, indicates the peak temperature is located in the aqueous solution near the FTO substrate. This suggests that the MW energy is delivered directly to the aqueous solution via dielectric heating, and the presence of conductive FTO glass also contributes by resistive heating, from physical movement of charge polarised by the MW. In contrast, with the conventionally heated CBD method, Fig. 1B, heat was transferred through the glass vessel resulting less effective of heating of the reaction solution. If the difference between conventional CBD and our URMAD is only limited to the heat transfer rate, one would not expect significant difference in the growth kinetics as we observed here. This confirms that the FTO layer behaves as an antenna which focuses the MW energy, resulting in the rapid growth using the microwave.

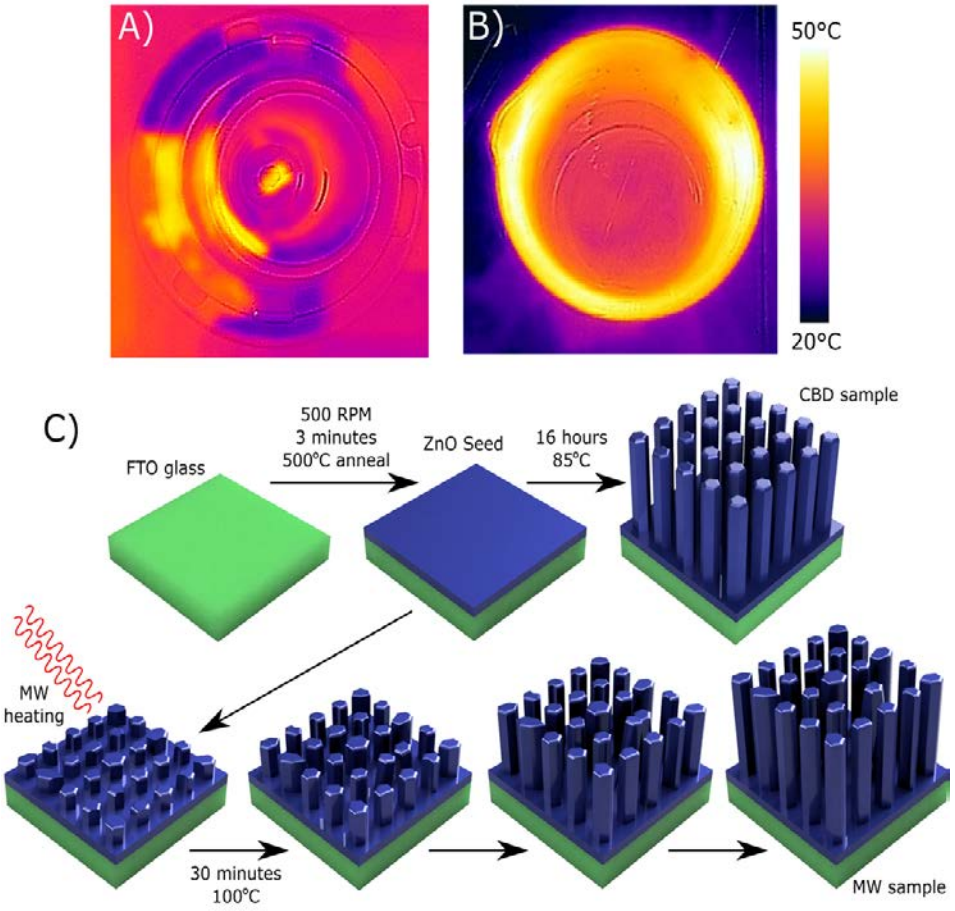


Figure 1: Thermal images of the solutions in A) the MW and B) the CBD processes with an FTO-glass inside. C) A schematic diagram shows both the CBD and URMAD methods.

A high surface area photoanode is important for highly efficient PEC water splitting, which allows faster faradaic charge transfer from semiconductor to electrolyte. Fig. 2A shows the uniform hexagonal wurtzite crystal morphology of the NRs synthesised from the URMAD method. The average diameter of the NRs was determined to be 138 ± 22 nm comparable to the NRs synthesised using conventional CBD method (Fig. S1). A small fraction of the rods appears irregular in shape, occurring from the coalescing of rods due to their rapid growth rate. The vertical growth of the rods can be seen in the cross-section SEM image in Fig. 2B

with a thickness of 1.85 µm after total of 2 hours growth. The average growth rate is 0.93 µm $h^{-1}$, which is about 9 times faster than the conventional CBD method.

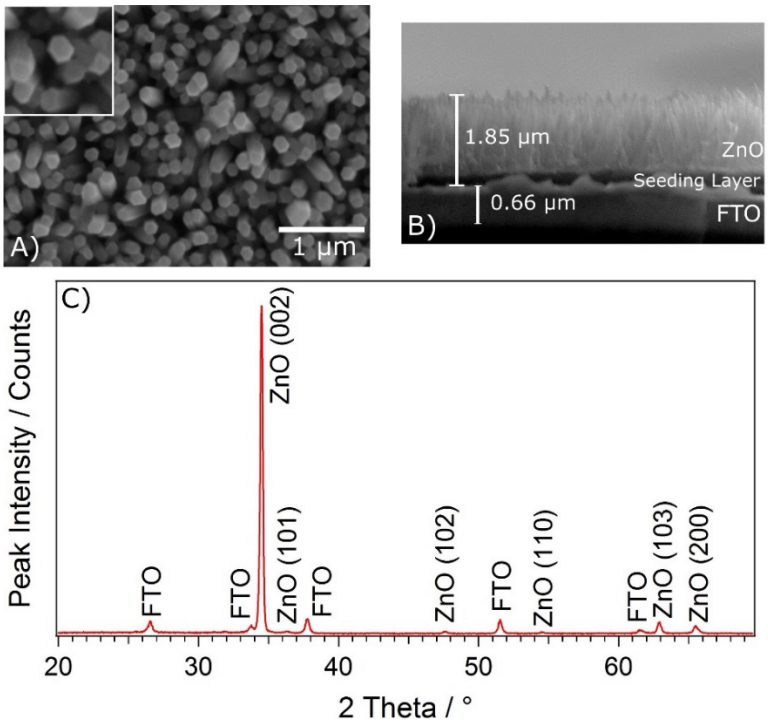


Figure 2: The top down and cross-sectional SEM images of the MW NRs can be seen in A) and B) respectively. The inset in A) shows the zoomed top view image. C) shows the XRD of the MW rods.

The ability to grow long ZnO NRs in a fraction of the time while maintaining the good quality morphology of conventional growth is important to their future use in solar energy. The vertically aligned growth of the wurtzite crystal structure is also evidenced with XRD, shown in Fig. 2C. The spectrum was indexed according to the standard database crystal patterns for wurtzite ZnO (JCPDS 36-1451). The dominant (002) peak confirms that the majority of this crystal planes are parallel to the substrate with a strong vertical alignment in the *c* axis.

### 3.2 PEC water splitting performance

The rapid growth rate in the URMAD process leads to high density of defects in the ZnO NRs and appropriate concentration of the defects could enhance the PEC performance. Evidence for the high density defects of the MW NRs can be analysed from the full width half maxima (FWHM) of the main (002) X-ray diffraction peaks, which is inversely proportional to the crystal domain size following the Scherrer equation.[42]

The high resolution (002) XRD peaks are displayed in Fig. S2. The measured peak widths from the CBD and URMAD NRs, as well as the samples annealed at different temperatures are presented in Fig. 3A. The CBD sample has the largest crystal domain size with the smallest diffraction peak width of 0.18° and the synthesized MW sample has the smallest crystal domain size with the largest peak width of 0.22°. Thus, one could expect that the URMAD samples will have a relatively high density of defects in the form of oxygen vacancies ($V_O$) and zinc interstitials ($Zn_i$). Annealing the MW sample in air at different temperatures will affect the defect density of the NRs. A systematic reduction of peak width can be observed when the sample is thermally annealed at the temperature above 400°C. Under such conditions, both the densities of $V_O$ and $Zn_i$ at the NR surfaces were significantly reduced by the reaction with hot air.

Alongside peak width reduction there was also a systematic shift in peak position (Fig. S2) corresponding to a decrease in crystal lattice spacing. The calculated c-axis lattice constants for different samples are also shown in Fig. 3A. High density of defects can lead to increased spacing as interstitial atoms and charged vacancies deform the lattice. The MW sample displays the largest c axis spacing at 5.206 Å, compared with 5.200 Å in the CBD

sample likely due to this effect. This spacing is reduced with the temperature of annealing following a similar trend to FWHM, confirming the effect of defect population.

The direct electronic band gap energies, $E_g$, of the ZnO NR arrays are also correlated to the density of defects. Native defects acting as dopants introduce new states into the electronic band structure of materials, if these states lie within the band gap of semiconductors it can lead to an effective reduction in band gap energy.[43] The values of $E_g$ displayed in Fig 3B, were determined using UV-Vis absorption spectroscopy and Tauc plots (Fig. S3).[44] For the MW sample, the band gap energy was 3.19 eV, which is a significant red shift from the 3.28 eV for the CBD sample in association with the high defect density. Such a decrease would allow the ZnO to absorb the leading edge of the visible spectrum which enhances its photocatalytic activity.[11] The effect of thermal annealing on the MW NRs is as expected, increasing the band gap energy approaching the $E_g$ of the CBD sample as $V_O$ and $Zn_i$ are reduced during the annealing process.

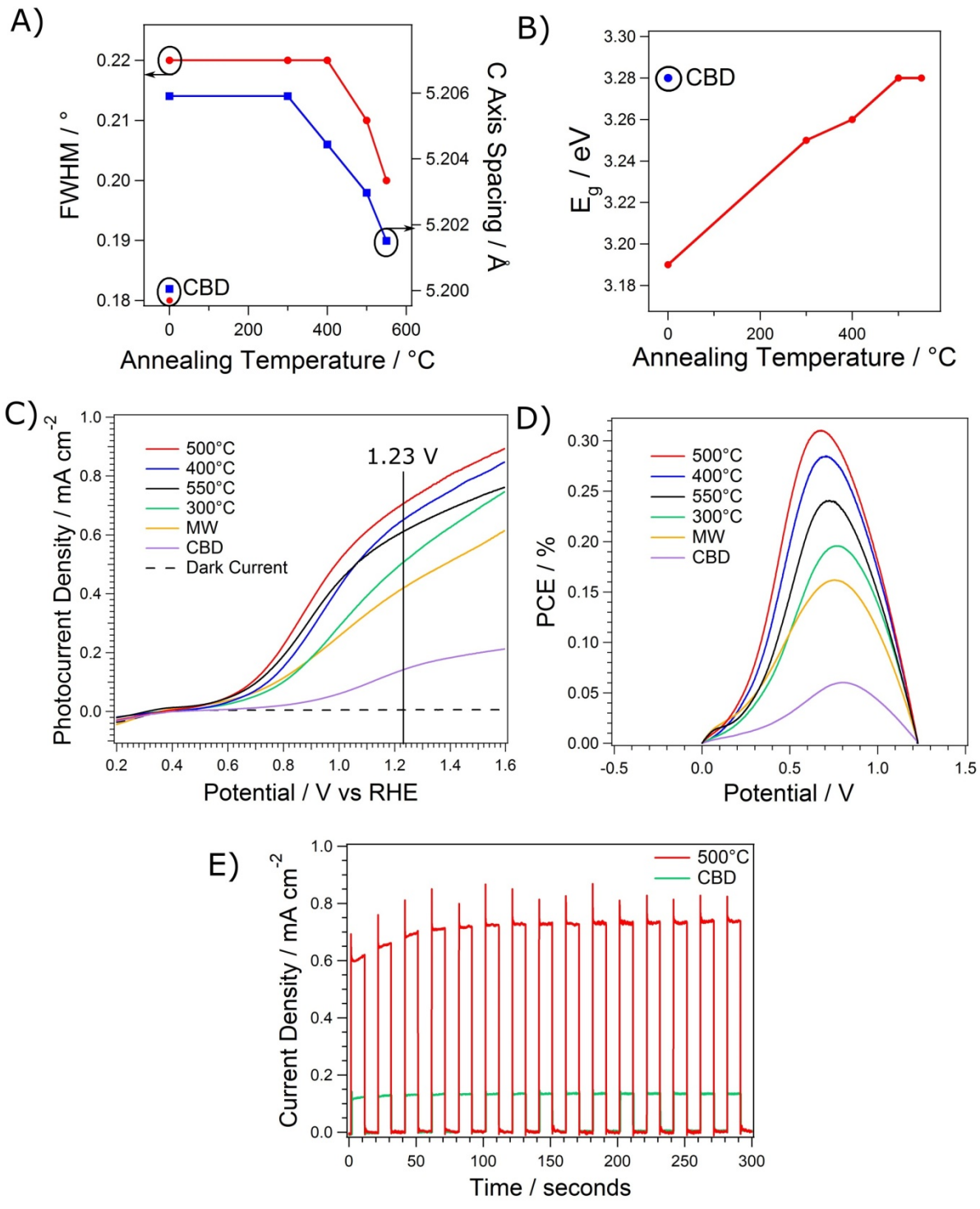


Figure 3: A) Displays the FWHM of (002) ZnO wurtzite peak of the samples against annealing temperature, along with lattice parameter c. B) Shows the evolution of band gap

energy with annealing temperature. Water splitting data showing C) photocurrent densities and D) photoconversion efficiency curves. E) Shows the time dependent photocurrent for CBD and MW samples measured at 1.23 $V_{RHE}$.

The photocatalytic activity of the URMAD ZnO NRs with a high density of defects was investigated in PEC water splitting. In comparison with low defect density CBD NRs, a much higher PEC water splitting activity was observed from the URMAD NRs, shown in Fig. 3C and D. At a potential bias of 1.23 $V_{RHE}$, the photocurrent of 0.420 mA $cm^{-2}$ was achieved from the MW samples with respect to the 0.140 mA $cm^{-2}$ from the CBD sample, although both have almost identical nanostructures. This was then further improved to 0.705 mA $cm^{-2}$ by thermal annealing at 500°C. Careful analysis of the effects of annealing temperature reveals a monotonic increasing in the photocurrent from 300 to 500°C, at which the maximum photocurrent was achieved. Further increasing the annealing temperature to 550°C, the photocurrent decreased to 0.601 mA $cm^{-2}$. The achieved photocurrent from the MW NRs is also greater than the reported Na doped ZnO NRs of 0.480 mA $cm^{-2}$ at 1.23 $V_{RHE}$.[11] Similar but lower photocurrent (0.600 mA $cm^{-2}$ at 1.23 $V_{RHE}$) was achieved from the hydrothermal synthesised ZnO NRs by Baek *et al*.[45] Their synthetic process took 12 hours and their sample was annealed at 700°C under vacuum which could increase the defect density of the ZnO NRs significantly. To prove the current is contributed from the photoexcitation process, the light chopped I-V curves for the as synthesised MW sample, the annealed MW sample and the CBD sample are demonstrated in Fig. S4.

The corresponding photoconversion efficiencies were plotted in Fig. 3D. A similar trend can be found as the photocurrent and best photoconversion performance was achieved from

the MW sample annealed at 500°C with maximum photoconversion efficiency of 0.31%, which is 5 times higher, with respect to the value from the CBD NRs (0.06%). Annealing at 550°C leads to a decrease as too many of the n-type impurities have been lost, which reduces the electron conductivity.

The chemical stability and the lifetime of the photoanode are crucial in practical applications. Shown in Fig. 3E, the time dependent photocurrent was recorded for a duration of 300 sec at a fixed positive bias of 1.23 $V_{RHE.}$ For clarity, the illumination light was chopped during measurement. For both CBD and MW samples, there is no observed photocurrent decrease. This confirms the stability of the MW photoanode.

In a wider review of pristine ZnO nanostructures found in Fig. S5, photoanode performance, measured by photocurrent density at 1.23 $V_{RHE}$, was compared to the literature. This work was found to be one of the fastest processing times compared with the prior art, only slower than one hydrothermal method[46] and glancing angle electron beam deposition thin films.[6] However, the water splitting photocurrents of these samples were an order of magnitude lower than ours. In fact, the PEC performance of our optimised MW ZnO NRs is among the best reported in literature.[14,45,47] Vuong *et al.* achieved a slightly higher photocurrent of ~0.9 mA $cm^{-2}$ from their hydrothermal synthesised ZnO NRs, with a special rapid scan rate of 50 mV $s^{-1}$ (relative to 10 mV $s^{-1}$ commonly used).[14] Nevertheless, their synthetic method is much slower than our URMAD method.

### 3.3 Density of defects and their effects on PEC performance

A high density of defects could affect the PEC efficiency in two opposite ways, depending on their concentration, location and function. Defects in semiconductors generate additional electronic states between the band gap, which can increase the dopant density of the material. The surface defects form recombination centers, which trap excited charges. A high density of such defects could decrease the PEC performance. Secondly, the bulk defects help to improve the electron conductivity without significant increase in charge recombination, thus enhancing the PEC performance. With a high density of recombination centers, the excited electrons and holes recombine and emit photoluminence (PL) signal. Therefore, one can use the PL signal to study the samples' relative defect density. Fig. 4A shows the thin film PL signals from different samples, excited at 320 nm. There are 5 major PL peaks located at the wavelengths of 397, 421, 446, 486 and 528 nm. The first peak found at 397 nm corresponds to the Near Band Edge (NBE) emission,[48] defined by the band gap energy of 3.18 eV. The intensity of this peak is proportional to the natural pathway of recombination of electron hole pairs. The peak at 421 nm can be attributed to the donor level associated with $Zn_i$,[49,50] while the two peaks centred at 446 and 486 nm arise from two different electronic states of $V_O$.[8,51] Finally, the 528 nm peak is reported to originate from $V_{Zn}$, an acceptor defect.[49,52,53]

The defect density of ZnO has been controlled by changing the reactant concentration or post annealing. Cui *et al.* controlled the defect density by altering the concentration of HMT in the growth solution.[54] Post annealing was also used to reduce surface defects in the form of

hydroxyl groups which achieved significant enhancement in the water splitting efficiency.[45]

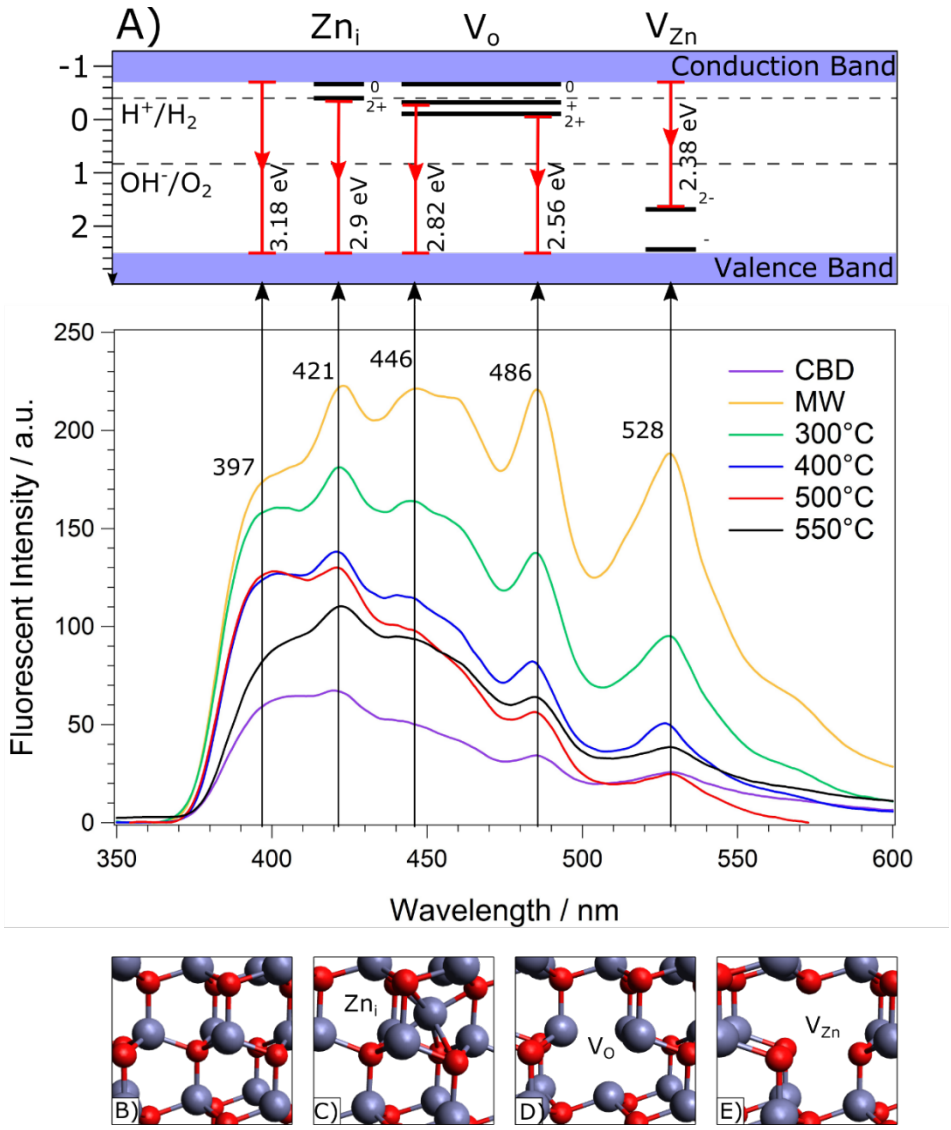


Figure 4: A) displays Forbidden zone band structure with electronic transitions indicated (top) and PL spectra of different samples (bottom) with peak positions in nm and C-F) diagrams of crystal defects.

Furthermore, Zeng *et al.* controlled the blue defect emission attributed to $Zn_i$ defects by annealing in both air and $N_2$ environments, reducing and increasing its abundance

respectively.[55] Annealing in air was, therefore, selected to reduce the defect density in the defect rich microwave samples in this study.

The difference in the PL emission from URMAD to CBD sample confirms the rapidly grown samples contain a high density of defects, since the CBD sample has much lower PL intensity. The coexistence of $Zn_{i,}$ $V_O$ and $V_{Zn}$ defects, suggests that both Frenkel and Schottky defects were formed during the URMAD process. The rapid decomposition of HMT in the MW will cause the fast increase of the solution pH. This results in the fast conversion of $Zn(NO_3)_2$ into $Zn(OH)_2$ and the formation of ZnO with less time to remove the crystal defects. The PL intensity was gradually reduced with thermal annealing in air up to 500°C. This suggests that the defect densities of all types, including $Zn_{i,}$ $V_O$ and $V_{Zn,}$ are significantly reduced through the diffusion and reactions starting from NR surface.[49] In particular, the population of the Frenkel defects was decreased through the annihilation of $Zn_i$ and $V_{Zn,}$ while the Schottky defects were reduced by the reaction between $V_O$ and $V_{Zn}$. However, with annealing temperature reaching 550°C, the PL signal at 528 nm, assigned to the $V_{Zn}$ species increases. This can be explained in that the corresponding thermal energy at 550°C exceeds the energy barrier for dissociating the Zn-O bonding within the ZnO lattice, allowing the displacement of $Zn^{2+}$, creating $V_{Zn}$.[52] The slight increase in the 486 nm peak suggests that paired $V_O$ also formed under these conditions. Therefore, additional Schottky defects were formed at high temperature. TEM images of the CBD and URMAD synthesised ZnO nanorods are shown in Fig. S6, where some crystal defects can be observed from the URMAD sample while the CBD sample shows relatively fewer.

EIS was recorded with a sinusoidal AC modulated (1 kHz, 10 mV) DC potential scanning from -0.6 to 0.6 V vs Ag/AgCl. The measured capacitance was used to produce Mott-Schottky (MS) plots in order to probe the flat band potential, and vitally, the density of dopants in the NR crystals. By plotting $\frac{1}{C^2}$ against DC bias, the key values of $N_D$, the dopant density, is determined from the inverse of the gradient of the linear section of the plot and $V_{FB}$, the flat band potential can be obtained from its intercept.[56,57] $N_D$ measures the excess concentration of n-type or p-type dopants in the sample. Greater populations of charge carriers lead to faster charge transfer and greater conductivity.

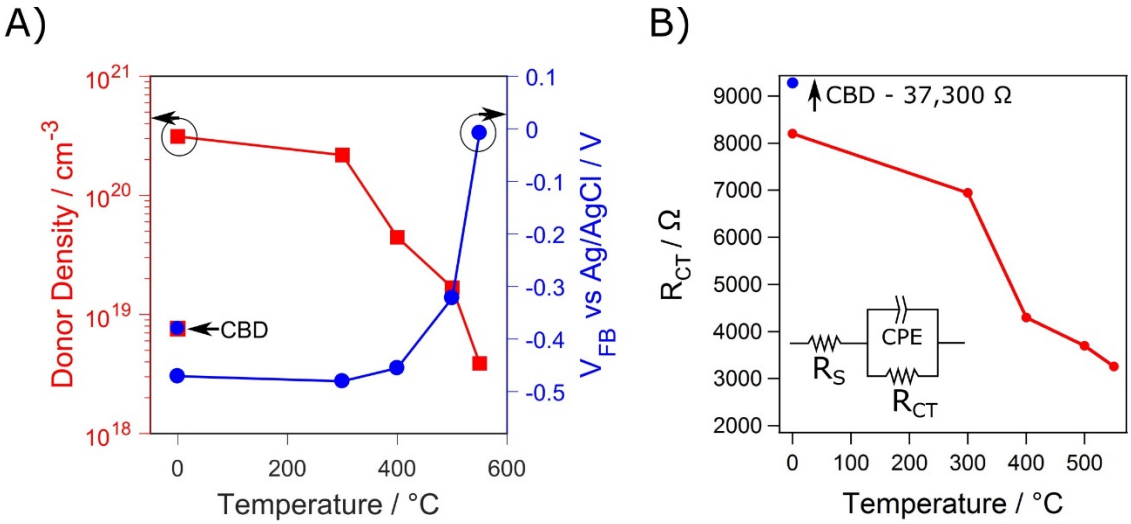


Figure 5: Donor density is shown on a logarithmic scale in A) with the flat band potential against annealing temperature. Charge transfer resistance, $R_{CT}$, vs annealing temperature is shown in B), inset shows Randles circuit with constant phase element (CPE), $R_{CT}$ and series resistance ($R_S$) elements.

The measured MS plots are shown in Fig. S7 and the obtained $N_D$ and $V_{FB}$ are plotted in Fig. 5A. An increase of two orders of magnitude in n-type dopant density to $3.12 \times 10^{20}$ $cm^{-3}$

is observed in the MW sample compared to $7.61 \times 10^{18}$ $cm^{-3}$ for a CBD sample. This is directly related to the rapid synthesis of the URMAD. The associated defects are likely to be $V_O$ and $Zn_i$, as identified in our PL measurements in Fig. 4.

By annealing the sample from 300°C to 550°C, the dopant density of the URMAD sample is reduced monotonically, reflecting a significant reduction in n-type doping ($V_O$ and $Zn_i$) with temperature, as annealing with increased temperature in air would lead to the healing of crystal structure, also observed by PL spectroscopy. In the annealing process, the surface defects will be significantly reduced initially, since they are in direct contact with air. The reduction in the surface Frenkel defect density leads to a reduction in recombination rate, which results in improved water splitting performance up to 500°C. Annealing at 550°C led to a further reduction of net dopant density which is lower than the CBD sample. This could be the result of either the reduction of n-type dopant ($V_O$ and $Zn_i$), or the increase of p-type dopant ($V_{Zn}$). The PL observation confirms the later is the dominant effects for the sample annealed at 550°C. The increase in the p-type dopant ($V_{Zn}$) will trap the holes and create extra energy barriers for the transportation of surface holes to facilitate the oxidation of $H_2O$ and thus the decrease of the PEC performance.

The flat band potentials from the MS analysis are also plotted in Fig. 5A. The measured $V_{FB}$ are typical for ZnO materials, with values varying from -0.59 V[58] to 0.03 V[9] vs Ag/AgCl in identical electrolyte.[21] A dramatic increase in $V_{FB}$ is observed due to the reduction of n-type dopants in the ZnO NRs during the annealing process. With a reduction in n-type doping, the flat band potential descends towards the valence band.[57,59] Similar effects have been explained by the Moss-Burstein relation.[60–62] The significant shift of the $V_{FB}$ for the 550°C annealed

sample is due to the population increase in $V_{Zn}$, an acceptor impurity, increasing the p-type doping in the sample. Such upper shift of the $V_{FB}$ will significantly reduce the reduction power of the photoexcited electrons in the conduction band, resulting in the limitation of the PEC performance.

The URMAD synthesised samples have a high density of donor defects, which are responsible for charge trapping and electron-hole recombination. Annealing the samples at mild temperature reduces the donor concentration and improves the PEC performance. However, by annealing the sample at high temperature, the concentration of acceptor starts to increase. Such acceptors, in the form of $V_{Zn}$, can trap holes in the valence band and reduce the reduction potential of the excited electrons in the conduction band due to the increase in the $V_{FB}$. Our experiment shows that the optimum condition is to anneal the URMAD sample at 500°C yielding optimum dopant density of $1.68 \times 10^{19}\,cm^{-3}$. It is clear, that any existence of accepters in the ZnO will significantly reduce the PEC performance.

Varying the AC frequency from 10 kHz to 0.1 Hz at a constant voltage bias of 0 V vs Ag/AgCl under illuminated conditions allowed the interface resistance and charge recombination rate of the samples to be analysed. The result is displayed in a Nyquist plot of imaginary vs real impedance (Fig. S8). In order to determine the critical value of charge transfer resistance, $R_{CT}$, the Nyquist plot is fitted with a standard Randles circuit model.[63] As there are no distinct frequency regions in the Nyquist plot, the values of $R_{CT}$ represent resistance at the liquid/solid interface as the resistance in the bulk semiconductor is far lower in comparison.[64] A lower $R_{CT}$ indicates less resistance for charge moving via faradaic charge transfer through this junction resulting a rapid charge transfer or lower recombination

resistance at the junction.[65] In Fig. 5B, $R_{CT}$ is plotted against annealing temperature with a stark difference from 37.3 kΩ for the CBD sample to 8.2 kΩ for the MW sample. This explains the PEC performance increase in the MW sample as charges are more efficiently transferred at the electrolyte-ZnO interface.

The $R_{CT}$ values decrease monotonically with annealing temperature. This is likely due to the healing of surface defects, as confirmed by PL measurement and MS analysis. This would systematically reduce the recombination resistance at this junction as less charge is lost and more is transferred, further explaining the increase in solar water splitting efficiency. Despite the loss of $V_O$ and $Zn_i$ at the surface, many of the bulk defects remain providing good conductivity. At 550°C, despite the lowest $R_{CT}$, the addition of p-type Schottky doping becomes the dominant factor for the decreasing in PEC performance, as the flat band potential shifts towards the valence band.

## 4 Conclusion

We demonstrate a novel ultra rapid microwave assisted synthetic method for the production of ZnO NR arrays. For the first time MW ZnO NR arrays are applied to PEC water splitting with significantly high efficiency. The inclusion of a high population of crystal defects has led to an increase in n-type doping and a significant enhancement in water splitting. The most likely defects responsible are $Zn_i$ and $V_O$ determined by the PL measurements. The populations of defects were successfully controlled using thermal annealing in air. EIS measurements showed a dramatic reduction in the surface Frenkel defects of n-type dopant, with increasing annealing temperature. The dopant density was optimised from thermal annealing in air at 500°C. This led to a fivefold increase in

photoconversion efficiency from the CBD sample. Further increasing the annealing temperature to 550°C led to a higher concentration of $V_{Zn}$, a p-type dopant, which behaves as a hole trap and shifts the flat band potential towards the valence band. This in turn led to a reduction in the PEC performance.

**Supporting Information Available**:

SEM images of the CBD sample, expanded XRD spectra, UV-Vis absorption spectra with corresponding Tauc plots, light chopped I-V curves, a review of performances vs processing time, TEM images, Mott Schottky Plots and Nyquist Plots can be found in the supporting information.

## References


(1) Millar, R. J.; Fuglestvedt, J. S.; Friedlingstein, P.; Rogelj, J.; Grubb, M. J.; Matthews, H. D.; Skeie, R. B.; Forster, P. M.; Frame, D. J.; Allen, M. R. Emission Budgets and Pathways Consistent with Limiting Warming to 1.5 °C. *Nat. Geosci.* **2017**, *10* (10), 741–747.

(2) IPCC. Summary for Policymakers of IPCC Special Report on Global Warming of 1.5ºC approved by governments http://www.ipcc.ch/report/sr15/ (accessed Oct 8, 2018).

(3) Fujishima, A.; Honda, K. Electrochemical Photolysis of Water at a Semiconductor Electrode. *Nature* **1972**, *238* (5358), 37–38.

(4) Walter, M. G.; Warren, E. L.; McKone, J. R.; Boettcher, S. W.; Mi, Q.; Santori, E. A.; Lewis, N. S. Solar Water Splitting Cells. *Chem. Rev.* **2010**, *110* (11), 6446–6473.

(5) Chen, X.; Shen, S.; Guo, L.; Mao, S. S. Semiconductor-Based Photocatalytic Hydrogen Generation. *Chem. Rev.* **2010**, *110* (11), 6503–6570.

(6) Wolcott, A.; Smith, W. A.; Kuykendall, T. R.; Zhao, Y.; Zhang, J. Z. Photoelectrochemical Study of Nanostructured ZnO Thin Films for Hydrogen Generation from Water Splitting. *Adv. Funct. Mater.* **2009**, *19* (12), 1849–1856.

(7) Mishra, P. R.; Shukla, P. K.; Srivastava, O. N. Study of Modular PEC Solar Cells for Photoelectrochemical Splitting of Water Employing Nanostructured TiO2 Photoelectrodes. *Int. J. Hydrogen Energy* **2007**, *32* (12), 1680–1685.

(8) Janotti, A.; Van de Walle, C. G. Fundamentals of Zinc Oxide as a Semiconductor.

*Reports Prog. Phys.* **2009**, *72* (12), 126501.

(9) Cai, L.; Ren, F.; Wang, M.; Cai, G.; Chen, Y.; Liu, Y.; Shen, S.; Guo, L. V Ions Implanted ZnO Nanorod Arrays for Photoelectrochemical Water Splitting under Visible Light. *Int. J. Hydrogen Energy* **2015**, *40* (3), 1394–1401.

(10) Lee, H. J.; Shin, S. H.; Nam, K. T.; Nah, J.; Lee, M. H. Spontaneously Polarized Lithium-Doped Zinc Oxide Nanowires as Photoanodes for Electrical Water Splitting. *J. Mater. Chem. A* **2016**, *4* (9), 3223–3227.

(11) Lee, W. C.; Canciani, G. E.; Alwhshe, B. O. S.; Chen, Q. Enhanced Photoelectrochemical Water Oxidation by Zn x M y O (M = Ni, Co, K, Na) Nanorod Arrays. *Int. J. Hydrogen Energy* **2016**, *41* (1), 123–131.

(12) Mukhopadhyay, S.; Mondal, I.; Pal, U.; Devi, P. S. Fabrication of Hierarchical ZnO/CdS Heterostructured Nanocomposites for Enhanced Hydrogen Evolution from Solar Water Splitting. *Phys. Chem. Chem. Phys.* **2015**, *17* (31), 20407–20415.

(13) Li, X.; Li, J.; Cui, C.; Liu, Z.; Niu, Y. PbS Nanoparticle Sensitized ZnO Nanowire Arrays to Enhance Photocurrent for Water Splitting. *J. Phys. Chem. C* **2016**, *120* (8), 4183–4188.

(14) Vuong, N. M.; Reynolds, J. L.; Conte, E.; Lee, Y.-I. H:ZnO Nanorod-Based Photoanode Sensitized by CdS and Carbon Quantum Dots for Photoelectrochemical Water Splitting. *J. Phys. Chem. C* **2015**, *119* (43), 24323–24331.

(15) Lu, J.; Wang, H.; Dong, S.; Wang, F.; Dong, Y. Effect of Ag Shapes and Surface Compositions on the Photocatalytic Performance of Ag/ZnO Nanorods. *J. Alloys Compd.* **2014**, *617*, 869–876.

(16) Zhou, G.; Xu, X.; Ding, T.; Feng, B.; Bao, Z.; Hu, J. Well–Steered Charge–Carrier Transfer in 3D Branched CuxO/ZnO@Au Heterostructures for Efficient Photocatalytic Hydrogen Evolution. *ACS Appl. Mater. Interfaces* **2015**, *7* (48), 26819–26827.

(17) Wu, M.; Chen, W. J.; Shen, Y. H.; Huang, F. Z.; Li, C. H.; Li, S. K. In Situ Growth of Matchlike ZnO/Au Plasmonic Heterostructure for Enhanced Photoelectrochemical Water Splitting. *ACS Appl. Mater. Interfaces* **2014**, *6* (17), 15052–15060.

(18) Zhang, C.; Shao, M.; Ning, F.; Xu, S.; Li, Z.; Wei, M.; Evans, D. G.; Duan, X. Au Nanoparticles Sensitized ZnO Nanorod@nanoplatelet Core-Shell Arrays for Enhanced Photoelectrochemical Water Splitting. *Nano Energy* **2015**, *12*, 231–239.

(19) Cai, L.; Ren, F.; Wang, M.; Cai, G.; Chen, Y.; Liu, Y.; Shen, S.; Guo, L. V Ions Implanted ZnO Nanorod Arrays for Photoelectrochemical Water Splitting under Visible Light. *Int. J. Hydrogen Energy* **2015**, *40* (3), 1394–1401.

(20) Wang, M.; Ren, F.; Zhou, J.; Cai, G.; Cai, L.; Hu, Y.; Wang, D.; Liu, Y.; Guo, L.; Shen, S. N Doping to ZnO Nanorods for Photoelectrochemical Water Splitting under Visible Light: Engineered Impurity Distribution and Terraced Band Structure. *Sci. Rep.* **2015**, *5* (1), 12925.

(21) Wang, M.; Ren, F.; Cai, G.; Liu, Y.; Shen, S.; Guo, L. Activating ZnO Nanorod Photoanodes in Visible Light by Cu Ion Implantation. *Nano Res.* **2014**, *7* (3), 353–364.

(22) Shao, S.; Jia, P.; Liu, S.; Bai, W. Stable Field Emission from Rose-like Zinc Oxide Nanostructures Synthesized through a Hydrothermal Route. *Mater. Lett.* **2008**, *62* (8–9), 1200–1203.

(23) Podrezova, L. V.; Porro, S.; Cauda, V.; Fontana, M.; Cicero, G. Comparison between

ZnO Nanowires Grown by Chemical Vapor Deposition and Hydrothermal Synthesis. *Appl. Phys. A* **2013**, *113* (3), 623–632.

(24) Cheng, X.; Cao, S.; Huan, Y.; Bai, Z.; Li, M.; Wu, H.; Zhang, R.; Peng, W.; Ji, Z.; Yan, X. The Synergetic Benefits of Passivation Layer and Catalytic Layer on Hematite for Efficient Water Splitting. *Energy Technol.* **2018**.

(25) Cao, S.; Yan, X.; Kang, Z.; Liang, Q.; Liao, X.; Zhang, Y. Band Alignment Engineering for Improved Performance and Stability of ZnFe 2 O 4 Modified CdS/ZnO Nanostructured Photoanode for PEC Water Splitting. *Nano Energy* **2016**, *24*, 25–31.

(26) Polshettiwar, V.; Nadagouda, M. N.; Varma, R. S. Microwave-Assisted Chemistry: A Rapid and Sustainable Route to Synthesis of Organics and Nanomaterials. *Aust. J. Chem.* **2009**, *62* (1), 16–26.

(27) Nadagouda, M. N.; Speth, T. F.; Varma, R. S. Microwave-Assisted Green Synthesis of Silver Nanostructures. *Acc. Chem. Res.* **2011**, *44* (7), 469–478.

(28) Kappe, C. O.; Dallinger, D.; Murphree, S. S. *Practical Microwave Synthesis for Organic Chemists*; Wiley-VCH Verlag GmbH & Co. KGaA: Weinheim, Germany, 2008.

(29) Wang, W.; Zhu, Y. Shape-Controlled Synthesis of Zinc Oxide by Microwave Heating Using an Imidazolium Salt. *Inorg. Chem. Commun.* **2004**, *7* (9), 1003–1005.

(30) Huang, J.; Xia, C.; Cao, L.; Zeng, X. Facile Microwave Hydrothermal Synthesis of Zinc Oxide One-Dimensional Nanostructure with Three-Dimensional Morphology. *Mater. Sci. Eng. B Solid-State Mater. Adv. Technol.* **2008**, *150* (3), 187–193.

(31) Ma, M. G.; Zhu, Y. J.; Cheng, G. F.; Huang, Y. H. Microwave Synthesis and

Characterization of ZnO with Various Morphologies. *Mater. Lett.* **2008**, *62* (3), 507–510.

(32) Zhu, Z.; Yang, D.; Liu, H. Microwave-Assisted Hydrothermal Synthesis of ZnO Rod-Assembled Microspheres and Their Photocatalytic Performances. *Adv. Powder Technol.* **2011**, *22* (4), 493–497.

(33) Uma Sangari, N.; Chitra Devi, S. Synthesis and Characterization of Nano ZnO Rods via Microwave Assisted Chemical Precipitation Method. *J. Solid State Chem.* **2013**, *197*, 483–488.

(34) Ocakoglu, K.; Mansour, S. A.; Yildirimcan, S.; Al-Ghamdi, A. A.; El-Tantawy, F.; Yakuphanoglu, F. Microwave-Assisted Hydrothermal Synthesis and Characterization of ZnO Nanorods. *Spectrochim. Acta Part A Mol. Biomol. Spectrosc.* **2015**, *148*, 362–368.

(35) Baruah, S.; Mahmood, M. A.; Myint, M. T. Z.; Bora, T.; Dutta, J. Enhanced Visible Light Photocatalysis through Fast Crystallization of Zinc Oxide Nanorods. *Beilstein J. Nanotechnol.* **2010**, *1*, 14–20.

(36) Sin Tee, T.; Chun Hui, T.; Wu Yi, C.; Chi Chin, Y.; Umar, A. A.; Riski Titian, G.; Hock Beng, L.; Kok Sing, L.; Yahaya, M.; Salleh, M. M. Microwave-Assisted Hydrolysis Preparation of Highly Crystalline ZnO Nanorod Array for Room Temperature Photoluminescence-Based CO Gas Sensor. *Sensors Actuators B Chem.* **2016**, *227*, 304–312.

(37) Harrison, S. E. Conductivity and Hall Effect of ZnO at Low Temperatures. *Phys. Rev.* **1954**, *93* (1), 52–62.

(38) Kohan, A. F.; Ceder, G.; Morgan, D.; Van de Walle, C. G. First-Principles Study of Native Point Defects in ZnO. *Phys. Rev. B* **2000**, *61* (22), 15019–15027.

(39) Reynolds, D. C.; Look, D. C.; Jogai, B.; Van Nostrand, J. E.; Jones, R.; Jenny, J. Source of the Yellow Luminescence Band in GaN Grown by Gas-Source Molecular Beam Epitaxy and the Green Luminescence Band in Single Crystal ZnO. *Solid State Commun.* **1998**, *106* (10), 701–704.

(40) Alam, M. J.; Cameron, D. C. Preparation and Properties of Transparent Conductive Aluminum-Doped Zinc Oxide Thin Films by Sol–gel Process. *J. Vac. Sci. Technol. A Vacuum, Surfaces, Film.* **2001**, *19* (4), 1642.

(41) Lee, W. C.; Fang, Y.; Kler, R.; Canciani, G. E.; Draper, T. C.; Al-Abdullah, Z. T. Y.; Alfadul, S. M.; Perry, C. C.; He, H.; Chen, Q. Marangoni Ring-Templated Vertically Aligned ZnO Nanotube Arrays with Enhanced Photocatalytic Hydrogen Production. *Mater. Chem. Phys.* **2015**, *149–150*, 12–16.

(42) Kara, I.; Yildiz, A.; Yildiz, G.; Dogan, B.; Serin, N.; Serin, T. Al and X (Sn, Cu, In) Co-Doped ZnO Nanocrystals. *J. Mater. Sci. Mater. Electron.* **2016**, *27* (6), 6179–6182.

(43) Kim, K. J.; Park, Y. R. Spectroscopic Ellipsometry Study of Optical Transitions in Zn1−xCoxO Alloys. *Appl. Phys. Lett.* **2002**, *81* (8), 1420–1422.

(44) Tauc, J. Optical Properties and Electronic Structure of Amorphous Ge and Si. *Mater. Res. Bull.* **1968**, *3* (1), 37–46.

(45) Baek, M.; Kim, D.; Yong, K. Simple but Effective Way To Enhance Photoelectrochemical Solar-Water-Splitting Performance of ZnO Nanorod Arrays: Charge-Trapping Zn(OH) 2 Annihilation and Oxygen Vacancy Generation by Vacuum

Annealing. *ACS Appl. Mater. Interfaces* **2017**, *9* (3), 2317–2325.

(46) Li, J.-M.; Cheng, H.-Y.; Chiu, Y.-H.; Hsu, Y.-J. ZnO–Au–SnO 2 Z-Scheme Photoanodes for Remarkable Photoelectrochemical Water Splitting. *Nanoscale* **2016**, *8* (34), 15720–15729.

(47) Lv, R.; Wang, T.; Su, F.; Zhang, P.; Li, C.; Gong, J. Facile Synthesis of ZnO Nanopencil Arrays for Photoelectrochemical Water Splitting. *Nano Energy* **2014**, *7*, 143–150.

(48) Yu, Q.; Fu, W.; Yu, C.; Yang, H.; Wei, R.; Sui, Y.; Liu, S.; Liu, Z.; Li, M.; Wang, G.; et al. Structural, Electrical and Optical Properties of Yttrium-Doped ZnO Thin Films Prepared by Sol–gel Method. *J. Phys. D. Appl. Phys.* **2007**, *40* (18), 5592–5597.

(49) Lin, B.; Fu, Z.; Jia, Y. Green Luminescent Center in Undoped Zinc Oxide Films Deposited on Silicon Substrates. *Appl. Phys. Lett.* **2001**, *79* (7), 943.

(50) Chen, C.; Yang, Q.-H.; Yang, Y.; Lv, W.; Wen, Y.; Hou, P.-X.; Wang, M.; Cheng, H.-M. Self-Assembled Free-Standing Graphite Oxide Membrane. *Adv. Mater.* **2009**, *21* (29), 3007–3011.

(51) Cheng, P.; Li, S.; Zhang, L.; Li, J. Characterization of Intrinsic Donor Defects in ZnO Ceramics by Dielectric Spectroscopy. *Appl. Phys. Lett.* **2008**, *93* (1), 111–114.

(52) Janotti, A.; Van De Walle, C. G. Native Point Defects in ZnO. *Phys. Rev. B - Condens. Matter Mater. Phys.* **2007**, *76* (16), 1–22.

(53) Sekiguchi, T.; Ohashi, N.; Terada, Y. Effect of Hydrogenation on ZnO Luminescence. *Jpn. J. Appl. Phys.* **1997**, *36* (Part 2, No. 3A), L289–L291.

(54) Cui, J. Defect Control and Its Influence on the Exciton Emission of Electrodeposited

ZnO Nanorods. *J. Phys. Chem. C* **2008**, *112* (28), 10385–10388.

(55) Zeng, H.; Duan, G.; Li, Y.; Yang, S.; Xu, X.; Cai, W. Blue Luminescence of ZnO Nanoparticles Based on Non-Equilibrium Processes: Defect Origins and Emission Controls. *Adv. Funct. Mater.* **2010**, *20* (4), 561–572.

(56) Memming, R. *Semiconductor Electrochemistry*; Wiley-VCH Verlag GmbH: Weinheim, Germany, 2000.

(57) Gelderman, K.; Lee, L.; Donne, S. W. Flat-Band Potential of a Semiconductor: Using the Mott–Schottky Equation. *J. Chem. Educ.* **2007**, *84* (4), 685.

(58) Allagui, A.; Alawadhi, H.; Alkaaby, M.; Gaidi, M.; Mostafa, K.; Abdulaziz, Y. Mott-Schottky Analysis of Flower-like ZnO Microstructures with Constant Phase Element Behavior. *Phys. Status Solidi Appl. Mater. Sci.* **2016**, *213* (1), 139–145.

(59) Hankin, A.; Alexander, J. C.; Kelsall, G. H. Constraints to the Flat Band Potential of Hematite Photo-Electrodes. *Phys Chem Chem Phys* **2014**, *16* (30), 16176–16186.

(60) Van Den Meerakker, J. E. A. M.; Meulenkamp, E. A.; Scholten, M. (Photo)Electrochemical Characterization of Tin-Doped Indium Oxide. *J. Appl. Phys.* **1993**, *74* (5), 3282–3288.

(61) Choi, B. .; Im, H. .; Song, J. .; Yoon, K. . Optical and Electrical Properties of Ga2O3-Doped ZnO Films Prepared by r.f. Sputtering. *Thin Solid Films* **1990**, *193–194* (PART 2), 712–720.

(62) Radecka, M.; Rekas, M.; Trenczek-Zajac, A.; Zakrzewska, K. Importance of the Band Gap Energy and Flat Band Potential for Application of Modified TiO2 Photoanodes in Water Photolysis. *J. Power Sources* **2008**, *181* (1), 46–55.

(63) Klahr, B.; Gimenez, S.; Fabregat-Santiago, F.; Hamann, T.; Bisquert, J. Water Oxidation at Hematite Photoelectrodes: The Role of Surface States. *J. Am. Chem. Soc.* **2012**, *134* (9), 4294–4302.

(64) Fabregat-Santiago, F.; Garcia-Belmonte, G.; Bisquert, J.; Zaban, A.; Salvador, P. Decoupling of Transport, Charge Storage, and Interfacial Charge Transfer in the Nanocrystalline TiO 2 /Electrolyte System by Impedance Methods. *J. Phys. Chem. B* **2002**, *106* (2), 334–339.

(65) Liu, Y.; Yan, X.; Kang, Z.; Li, Y.; Shen, Y.; Sun, Y.; Wang, L.; Zhang, Y. Synergistic Effect of Surface Plasmonic Particles and Surface Passivation Layer on ZnO Nanorods Array for Improved Photoelectrochemical Water Splitting. *Sci. Rep.* **2016**, *6* (1), 29907.

TOC image:

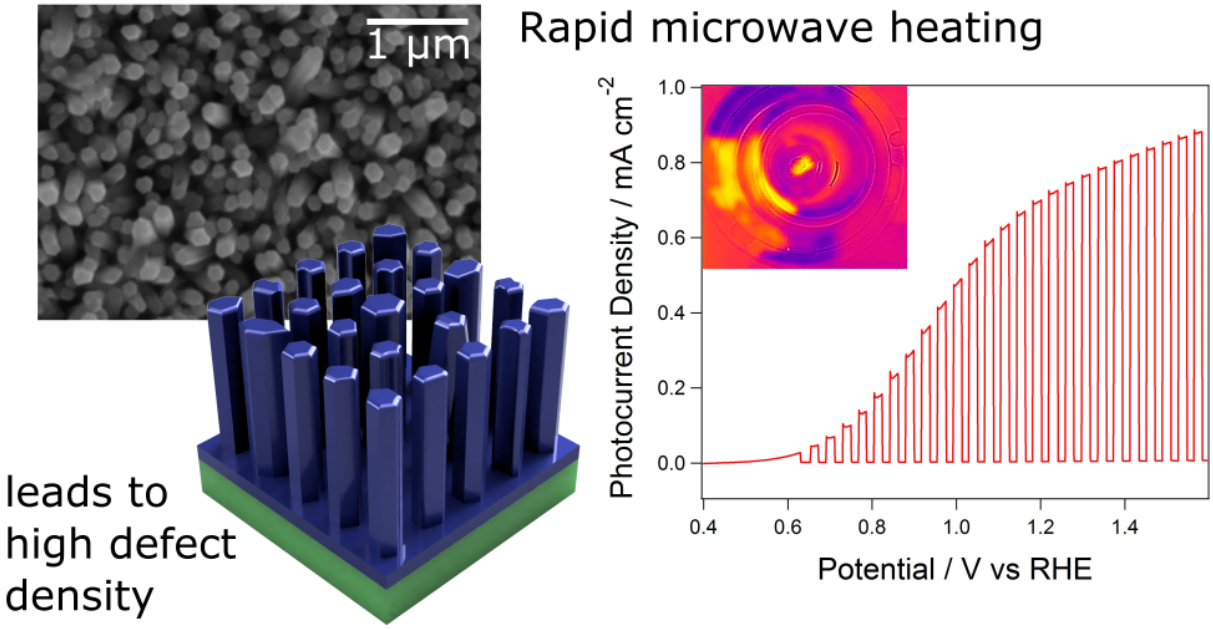
1 µm
Rapid microwave heating
leads to
high defect
density
Photocurrent Density / mA cm-2
1.0
0.8
0.6
0.4
0.2
0.0
0.4
0.6
0.8
1.0
1.2
1.4
Potential / V vs RHE